

Demonstrating Quantum Speed-Up with a Two-Transmon Quantum Processor.

Andreas Dewes

March 28, 2012

Contents

1	Introduction & Summary	11
1.1	Quantum Computing & Circuit Quantum Electrodynamics	11
1.2	Realizing a Two-Qubit Quantum Processor	13
1.3	Demonstrating Simultaneous Single-Shot Readout	14
1.4	Generating and Characterizing Entanglement	15
1.5	Realizing a Universal Two-Qubit Quantum Gate	19
1.6	Running a Quantum-Search Algorithm	20
1.7	Demonstrating Quantum Speed-Up	21
1.8	Designing a Scalable Quantum Computing Architecture	22
2	Theoretical Foundations	25
2.1	Quantum mechanics & Quantum Computing	25
2.2	Transmon qubits	25
2.3	Circuit quantum electrodynamics	26
2.3.1	Dispersive limit & qubit readout	27
2.4	The Josephson bifurcation amplifier	27
3	Realizing a Two-Qubit Processor	29
3.1	Introduction & Motivation	29
3.2	Processor Design	30
3.3	Processor Fabrication	31
4	Measurement Setup & Techniques	33
4.1	Measurement techniques	35

5	Processor Characterization	37
5.0.1	Spectroscopic measurements	37
	Qubit Parameters	37
	Readout Parameters	37
5.0.2	Readout	38
5.0.3	Single-Qubit Operations	38
5.0.4	Quantum State Tomography	38
	Maximum Likelihood Estimation	39
5.0.5	Two Qubit Operations	40
	Creation of Entanglement	40
	Violation of Bell's inequality	40
5.0.6	Characterizing Quantum Processes	40
	Introduction & Principle	40
	Implementation	40
	The Kraus representation	43
5.0.7	Realizing a Two-Qubit Gate	45
	Principle	45
	Implementation	45
	Fidelity	45
	Error Analysis	45
6	Running the Grover Search Algorithm	47
6.0.8	Introduction & Motivation	47
6.0.9	Experimental Implementation	48
6.0.10	Results	48
	Algorithm Fidelity	48
	Single-Run Probabilities	48
	Error Analysis	48
6.0.11	Conclusions	48
7	Scalable Architectures for Quantum Bits	51
7.1	Definition & Requirements	51
7.2	Qubit Design	51
7.3	Microwave Driving	51

<i>CONTENTS</i>	5
7.4 Frequency Manipulation	51
7.5 Readout	51
7.6 Coupling	51
7.7 A 4-Qubit Architecture	51
7.8 Scaling Up	51
8 Conclusions & Outlook	53
8.1 Future Directions in Superconducting QC	53
8.1.1 3D Circuit Quantum Electrodynamics	53
8.1.2 Hybrid Quantum Systems	53
8.1.3 Quantum Error Correction & Feedback	53
A Modeling of Multi-Qubit Systems	55
A.1 Analytical Approach	55
A.1.1 Multi-Qubit Hamiltonian	55
A.1.2 Energies and Eigenstates	55
A.2 Master Equation Approach	55
A.2.1 Direct Integration	55
A.2.2 Monte Carlo Simulation	55
A.2.3 Speeding Up Simulations	55
B Data Acquisition & Management	57
B.1 Data Acquisition Infrastructure	57
B.2 Data Management Requirements	57
B.3 PyView	57
B.3.1 Overview	57
B.3.2 Instrument Management	57
B.3.3 Data Acquisition	57
B.3.4 Data Management	57
B.3.5 Data Analysis	57
C Design & Fabrication	59
C.1 Mask Design	59
C.2 Optical Lithography	59
C.3 Electron Beam Lithography	59

D Bibliography**59**

List of Figures

1.1	Blueprint of a two-qubit quantum processor	11
1.2	Circuit schematic of the realized two-qubit processor	14
1.3	Switching probabilities of the two qubit readouts as a function of the read- out excitation power	15
1.4	Generating entangled two-qubit states by swapping interaction	16
1.5	Measurement of the CHSH operator of an entangled two-qubit state . . .	18
1.6	Measured χ -matrix of the \sqrt{i} SWAP gate	19
1.7	Schematic of the implementation of Grovers search algorithm	20
1.8	Measured density matrices when running Grover's algorithm	21
1.9	Single-run results of the Grover search algorithm	22
1.10	23
3.1	Circuit schematic of the two-qubit processor	30
3.2	Spectroscopy of the Two-Qubit Processor	31
4.1	The measurement setup used for the two-qubit experiments	34
5.1	38
5.2	41
5.3	41
5.4	test	45
5.5	46
6.1	Pulse sequence used for implementing Grovers search algorithm	48
6.2	49
6.3	50

List of Tables

Chapter 1

Introduction & Summary

1.1 Quantum Computing & Circuit Quantum Electrodynamics

This thesis presents experiments performed on a superconducting Two-Qubit quantum processor. The main goal of this work was to demonstrate a possible quantum computing architecture using superconducting qubits that follows the canonical blueprint of a Two-qubit quantum processor, as given by the four criteria of DiVincenzo (2000) and as shown in fig. 1.1. By this definition a universal quantum computer is a register of quantum bits – or qubits – on which one can perform universal single- and two-qubit quantum gates, read out the state of each qubit individually and with high fidelity and reset the qubit register to a well-defined state.

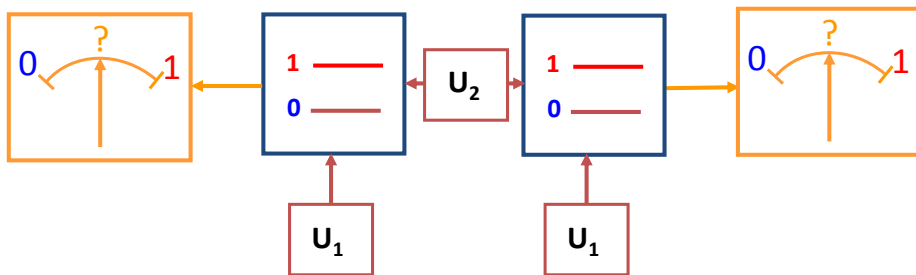


Figure 1.1: The blueprint of a two-qubit quantum processor. Shown are two qubits that can be individually manipulated (U_1) and are connected by a universal two-qubit gate U_2 . Each of the qubits can be read out individually.

Implementing this allegedly simple list of requirements in a system of superconducting qubits has been a major research challenge during the last decade. After the first demonstration of coherent quantum dynamics in a superconducting charge-based qubit by Nakamura et al. (1999), a broad research field on superconducting quantum bits has sprung up. In the years following Nakamura's initial experiment, several types of superconducting qubits were proposed and realized using e.g. the superconducting phase (Martinis et al., 1985, 2002) across a Josephson junction or the magnetic flux (Mooij et al., 1999; Chiorescu et al., 2003) inside a superconducting ring interrupted by one or several Josephson junctions as the dominant quantum variable. An important result on the way to robust superconducting qubits was the development of the so-called *Quntronium* qubit by Vion et al. (2002), which demonstrated for the first time a quantum-mechanical coherence time larger than $1 \mu s$ by operating a Cooper pair box at a sweet spot in a regime where the charging and Josephson phase energies of the system are of comparable value. This invention made it possible to perform for the first time robust, NMR-like quantum operations using a superconducting qubit (Collin et al., 2004). In 2004, the development of a new type of qubit, the so called *Transmon* by Wallraff et al. (2004) achieved again a drastic improvement by operating a Cooper pair box in the phase regime and thus rendering the resulting qubit almost insensitive to charge noise. In addition, by embedding the qubit in a superconducting coplanar waveguide (CPW) resonator it is possible to protect it from external sources of electrical noise and to use the shift of the resonance frequency of the resonator caused by a dispersive interaction with the qubit for reading out the qubit state (Blais et al., 2004). Using this so-called *circuit quantum electrodynamics* (CQED) architecture, quantum gates and algorithms with up to four qubits have been implemented, demonstrating multi-qubit entanglement (DiCarlo et al., 2010) and simple quantum algorithms (DiCarlo et al., 2009).

!1!

To Do 1: Think about moving the section on 3D-CQED directly after this one since this would probably be more logical

Question 1: Should I mention Michel here?

To Do 2: Add more citations here

To Do 3: Add reference to quantum feedback paper as soon as it appears

In parallel to this, the development of reliable quantum-limited amplifiers based on nonlinear superconducting resonators by ?1? I. Siddiqi (Siddiqi et al., 2004) complemented the CQED architecture by providing a fast and high-fidelity readout scheme for Transmon qubits (Siddiqi et al., 2006; Mallet et al., 2009) and for the amplification of quantum signals in general !2! . These quantum-limited amplifiers and detectors made it possible to directly observe quantum jumps in superconducting qubits (Vijay et al., 2011) and to implement quantum feedback in superconducting circuits !3! .

Recently, the development of a CQED architecture combining Transmon qubits with

3D superconducting resonator cavities instead of 1D coplanar waveguide resonators, as pioneered by Paik et al. (2011), resulted in an increase of qubit lifetimes of almost two orders of magnitude, with measured T_1 qubit relaxation times as high as $80 \mu\text{s}$!4! and decoherence times at a comparable time scale. This increase in coherence times made possible the realization of high-fidelity quantum gates and qubit readout schemes !5! as well as elemental quantum feedback and error correction schemes, thus bringing quantum computing using superconducting qubits almost within experimental reach. !6!

To Do 4: verify this!

To Do 5: add references!

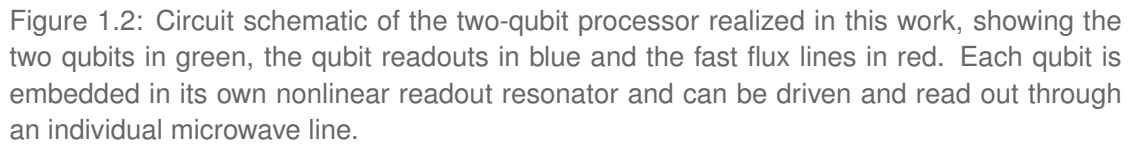
The research presented in this thesis wants to complement the CQED architecture by combining a multi-qubit architecture with a single-shot, individual-qubit readout scheme, thus aiming to develop a viable architecture for the implementation of a superconducting quantum computer using Transmon qubits.

To Do 6: expand this section as soon as new relevant material appears, include recent IBM, Yale

The first part of this thesis discusses therefore the realization of a superconducting quantum processor based on Transmon qubits and using an individual-qubit, single-shot readout scheme. We demonstrate elemental single- and two-qubit quantum operations on this processor and use it to implement a simple quantum algorithm that demonstrates quantum speed-up. Afterwards, we discuss the realization of a four-qubit quantum processor within a more scalable architecture that fulfills – to different degrees – all of the diVincenzo criteria and which could possibly be extended to a larger number of qubits.

1.2 Realizing a Two-Qubit Quantum Processor

The quantum processor implemented in this work is shown in fig. 1.2. It consists of two superconducting quantum bits of the Transmon-type, each equipped with its own drive and readout circuit. The qubit readout is realized by using a nonlinear coplanar-waveguide resonator which serves as a Josephson bifurcation amplifier (JBA) and allows a high-fidelity, single-shot readout of the qubit state. Each qubit can be manipulated by driving it with microwave pulses through its readout resonator, allowing robust single-qubit operations. In addition, the qubit frequencies can be tuned individually by fast flux lines, which allows us to change the frequency each qubit over a range of several GHz. The coupling between the two qubits is realized through a fixed capacitor that directly connects the two qubits and implements a fixed σ_{xx} -type qubit-qubit coupling. This allows to implement two-qubit gates and to generate entangled two-qubit states.



1.3 Demonstrating Simultaneous Single-Shot Readout

To read out the state of each qubit, a so-called Josephson bifurcation amplifier (Siddiqi et al., 2006; Mallet et al., 2009) is used. This readout works by capacitively coupling the qubit to a coplanar waveguide resonator which is rendered nonlinear by adding a Josephson junction at its center. This nonlinear resonator can exhibit bistable behaviour for certain drive parameters, which we use to map the state of the qubit to one of the bistable states of the resonator, thus obtaining a single-shot readout of the qubit state. In contrast to other CQED architectures, in our approach each of the qubits possesses its own JBA readout, allowing a simultaneous measurement of the state of the whole

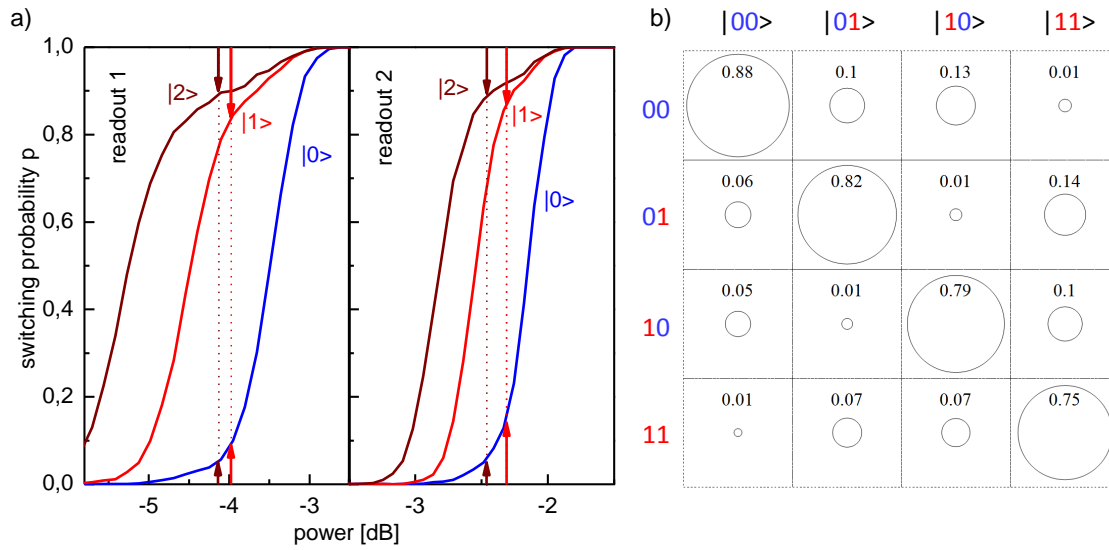


Figure 1.3: a) Switching probabilities of the two qubit readouts as a function of the readout excitation power. The measurement is performed after preparing the qubits in the states $|0\rangle$, $|1\rangle$ and $|2\rangle$. The readout fidelity is given as the difference in probability between the curves corresponding to the states $|0\rangle$ and $|1\rangle$ or $|2\rangle$, respectively. The highest readout fidelities of 88 and 89 % are achieved when the qubit is in state $|2\rangle$. b) Readout matrix of the two-qubit system. The matrix contains the probabilities of obtaining a given measurement result after having prepared the system in a given state. **Figure Comment 2: Replace this figure since it is not very intuitive. It would be better to show something which allows the reader to directly quantify the visibility and readout crosstalk present in the system.**

qubit register, thus following closely the canonical blueprint of a quantum computer as formulated by DiVincenzo. **!7!** Up to 93 % readout fidelity has been demonstrated using the JBA readout (Mallet et al., 2009), but due to design constraints the fidelity attained in the experiments discussed here was bound to 83-85 %, as shown in fig. 1.3. By measuring the simultaneous readout switching probabilities after initializing the qubit register in a given state we can extract and correct all readout errors.

To Do 7: discuss more details of the readout here...

1.4 Generating and Characterizing Entanglement

The fixed coupling between the two qubits provides a σ_{xx} -type coupling which is only effective when the qubit frequencies are nearly resonant. Therefore, it can be switched on and off by changing the qubit frequencies, which we use to implement two-qubit gates

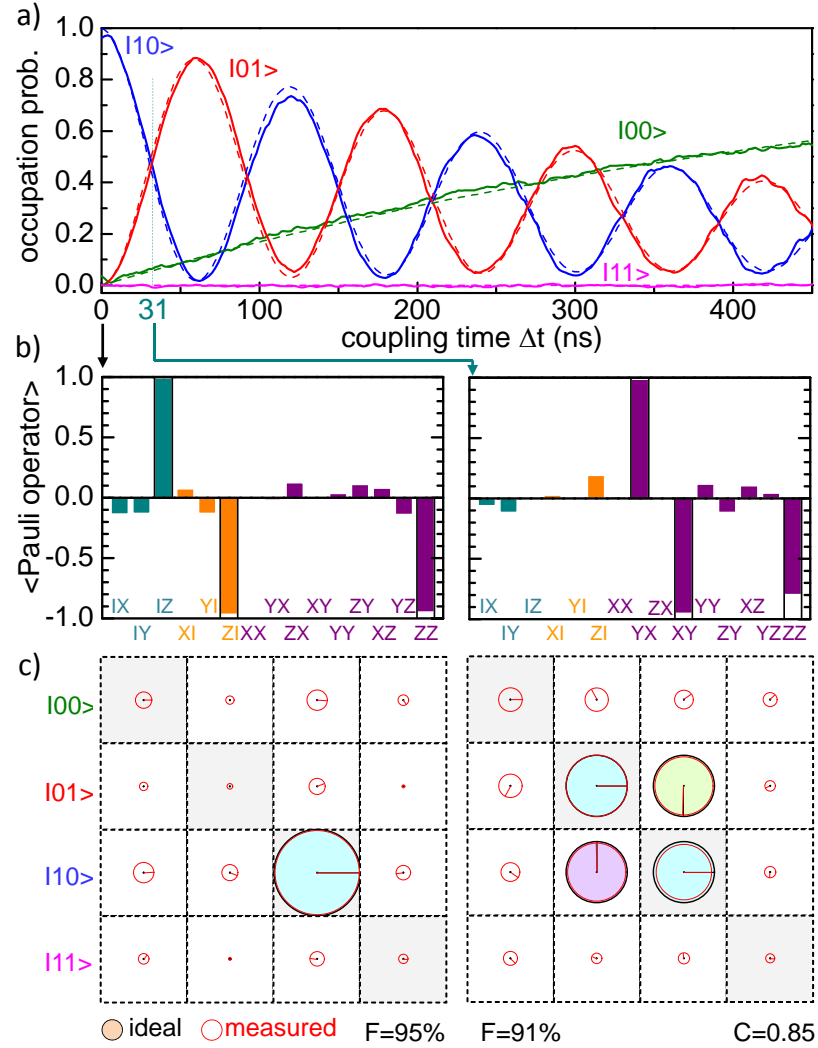


Figure 1.4: Energy oscillations between the two qubits induced by a resonant swapping interaction between them. a) The qubit state after switching on the swapping interaction for a given time Δt . The frequency of the oscillations corresponds to $2g = 8.7$ MHz. b) The Pauli set of the two-qubit state measured at 0 ns and 31 ns. c) The reconstructed density matrices corresponding to the two measured Pauli sets. In c), the area of each circle corresponds to the absolute value of each matrix element and the color and direction of the arrow give the phase of each element. The black circles correspond to the density matrices of the ideal states $|10\rangle$ and $1/\sqrt{2}(|10\rangle + i|01\rangle)$, respectively. **Figure Comment 4: verify sign!**

with this system. In our processor, the effective coupling constant g of the two qubits is given as $2g = 8.2$ MHz !8! . When using a fast fluxline pulse to abruptly tune the qubits in resonance we can switch on the qubit-qubit coupling non-adiabatically and generate an evolution operator of the form

To Do 8: Check if this is really $2g$!

$$U(t) = \begin{pmatrix} 1 & 0 & 0 & 0 \\ 0 & \cos 2\pi t g & i \sin 2\pi t g & 0 \\ 0 & i \sin 2\pi t g & \cos 2\pi t g & 0 \\ 0 & 0 & 0 & 1 \end{pmatrix} \quad (1.1)$$

Switching off this interaction after a time $t_{\pi/2} = 1/8g$ allows the creation of entangled qubit states and the implementation of a universal quantum gate, as will be explained later. Before doing this, we characterize the evolution of the qubits during the swapping interaction by preparing them in the state $|10\rangle$, switching on the interaction for a given amount of time and measuring the qubit state directly afterwards. The resulting curve shown in fig. 1.4 shows energy oscillations between the two qubits. Stopping the interaction after quarter of a period we obtain an entangled two-qubit Bell-type state that we can characterize by performing quantum state tomography. The experimental reconstruction of the density matrix of such a state corresponding approximating to the Bell-state $|\psi\rangle = 1/\sqrt{2}(|01\rangle + i|10\rangle)$ is shown in fig. 1.4b. The measured fidelity of this state of 91 % and the concurrence of 85 % confirms that entanglement is present in the system. This entanglement can also be characterized by measuring the so-called *Clauser-Horne-Shimony-Holt* operator (Clauser et al., 1969) on the produced state. This operator is given as

$$CHSH = QS + RS + RT - QT \quad (1.2)$$

with the operators Q, R, S, T being given as

$$\begin{aligned} Q &= \sigma_z^1 & S &= \sigma_z^2 \cdot \cos \phi + \sigma_x^2 \cdot \sin \phi \\ R &= \sigma_x^1 & T &= -\sigma_z^2 \cdot \sin \phi + \sigma_x^2 \cdot \cos \phi \end{aligned} \quad (1.3)$$

Here, the angle ϕ is a parameter that should be chosen in accordance to the phase of the Bell state on which the operator is applied.

The expectation value $\langle CHSH \rangle$ provides a test of the quantum-mechanical char-

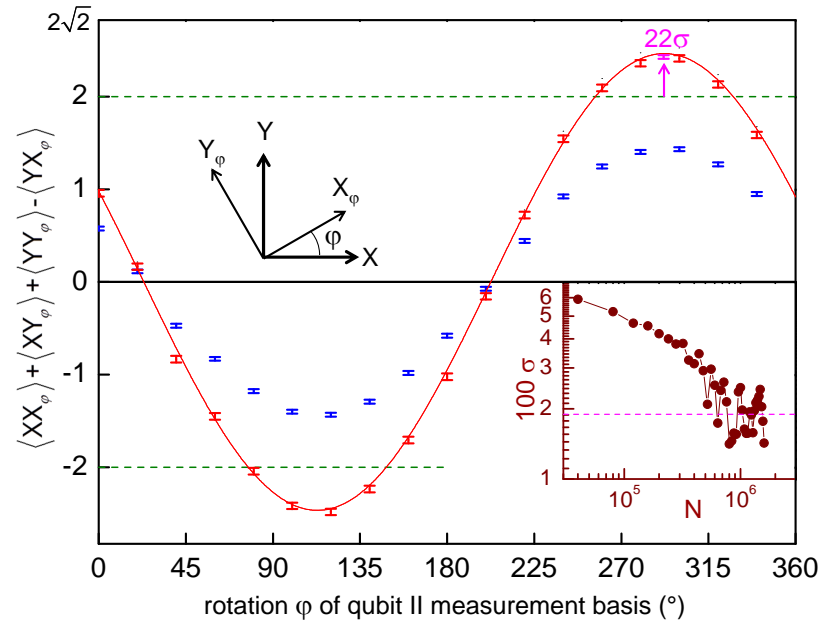


Figure 1.5: Measurement of the CHSH equation for an entangled two-qubit state. The renormalized CHSH expectation value (red points) exceeds the classical boundary of 2 by a large amount. The raw measurement data (blue points) lies below this critical threshold. The inset shows the standard deviation σ at the highest point of the curve as a function of the measurement sample size. For the highest sample count, the classical boundary is exceeded by 22 standard deviations. [Figure Comment 6: p. 140 in cavities 6 labbook](#)

acter of the generated state. For classical states, the maximum value is ≤ 2 but for entangled states it can reach a maximum value of $\sqrt{2} \cdot 2$. The result of a CHSH-type measurement performed on a state created by the method described above is shown in fig. 1.5, showing the value of $\langle CHSH \rangle$ as a function of ϕ . We observe a violation of the classical boundary 2 of the operator by 22 standard deviations when correcting readout errors present in our system. However, the raw, uncorrected data fails to exceed the non-classical bound, making it impossible to close the detection loophole with our system. Nevertheless the observed violation of the equation by the renormalized state is a strong indication of entanglement in the system.

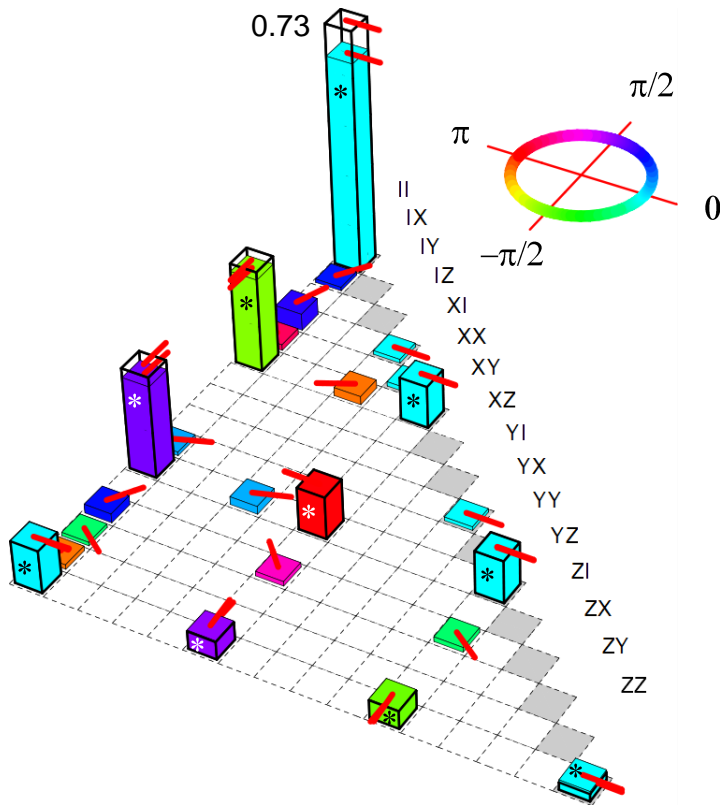


Figure 1.6: The measured χ -matrix of the implemented $\sqrt{i}\text{SWAP}$ gate. The row labels correspond to the indices of the E_i operators, the height of each bar to the absolute value of the corresponding matrix element and the color and direction of the red arrow to the complex phase of each element. The ideal χ -matrix of the $i\sqrt{\text{SWAP}}$ gate is given by the outlined bars. The upper half of the positive-hermitian matrix is not shown.

1.5 Realizing a Universal Two-Qubit Quantum Gate

The swapping evolution according to eq. (1.1) allows the implementation of a two-qubit gate. When switching on this interaction for $t_{\pi/2} = 1/8g$ we can realize the so-called $\sqrt{i}\text{SWAP}$ gate, which has the representation

$$\sqrt{i}\text{SWAP} = \begin{pmatrix} 1 & 0 & 0 & 0 \\ 0 & 1/\sqrt{2} & i/\sqrt{2} & 0 \\ 0 & i/\sqrt{2} & 1/\sqrt{2} & 0 \\ 0 & 0 & 0 & 1 \end{pmatrix} \quad (1.4)$$

and is a universal two-qubit quantum gate. The operation and errors of our implementation of this gate can be characterized by performing quantum process tomography, yielding a gate fidelity of 90 %. The 10 % error in gate fidelity is caused mainly by qubit relaxation and dephasing during the gate operation and only marginally by deterministic preparation errors, as will be discussed in the main text of the thesis. Fig. 1.6 show

the measured χ matrix of the implemented gate. The achieved fidelity of the gate operation is sufficient to allow the implementation of a simple quantum algorithm with our processor, as will be discussed in the following section.

1.6 Running a Quantum-Search Algorithm

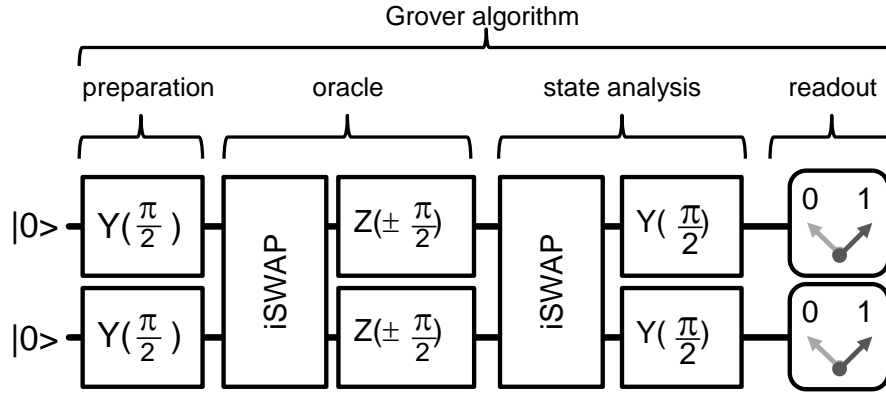


Figure 1.7: Schematic of the implementation of Grover's search algorithm on a two-qubit quantum processor. The algorithm consists in preparing a probe state, applying the quantum oracle to this state and analyzing the resulting output state to extract the information on the oracle operator.

In this work we use the quantum gate implemented above to run a compiled version of Grover's search algorithm (Grover, 1997). The implemented version of the algorithm works in the basis of two qubits $x_i \in \{|00\rangle, |01\rangle, |10\rangle, |11\rangle\}$ and can distinguish between four different *oracle functions* $f(x)$ that each tag on one of the basis states x_j . Since the Grover algorithm for 2 qubits requires only one evaluation of the function $f(x)$ to determine which state has been marked it is faster than any conceivable classical algorithm, thus demonstrating the concept of quantum speed-up. The schematic of our version of Grover's algorithm is shown in fig. 1.7 and involves two i SWAP gates and three single-qubit operations along with a single-shot qubit readout at the end of the algorithm. We implemented all steps of this algorithm with our two-qubit processor and performed quantum state tomography after each step to reconstruct the quantum state at different points in the algorithm. Fig. 1.8 shows the experimentally measured density matrices when running the algorithm with an oracle that marks the state $|00\rangle$. State tomographies

are shown after applying the generalized Hadamard transform, after applying the quantum oracle and after the final step of the algorithm. This reconstruction of the quantum state using quantum state tomography does not however allow to demonstrate quantum speed-up, which requires individual single-shot readout of the qubit register, which will be discussed in the following section.

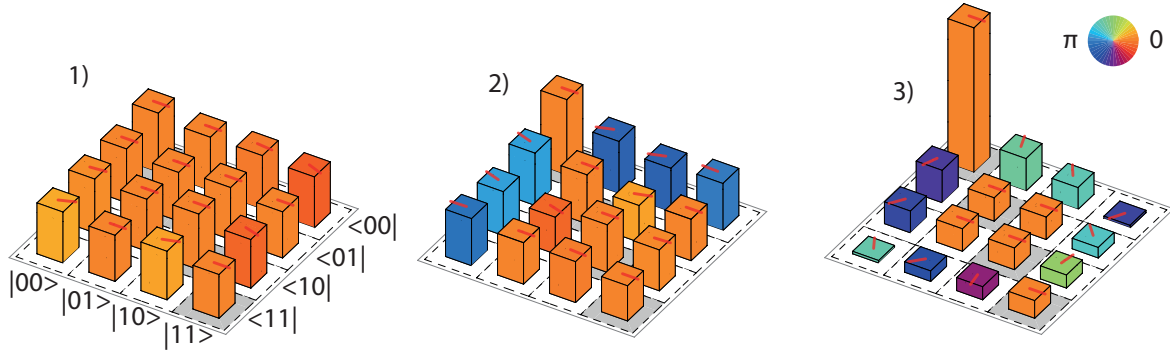


Figure 1.8: Measured density matrices when running Grover's search algorithm with a search oracle marking the state $|00\rangle$. 1) shows the state after the generalized Hadamard transform, 2) after applying the quantum oracle and 3) after the final step of Grover's algorithm.

1.7 Demonstrating Quantum Speed-Up

The main interest of running a quantum algorithm is to obtain an advantage in the run-time in comparison with a classical algorithm, the so-called *quantum speed-up*. To characterize this quantum speed-up as obtained with our processor, we run Grover's algorithm for all four possible oracle functions and directly readout out the qubit state after the last step of the algorithm, without correcting any readout errors. When averaging the results of such individual runs of the algorithm we can then obtain its single-run fidelity, which –for our processor– ranges between 52 and 67 %, depending on the state which is marked by the quantum oracle, as shown in fig. 1.9. These results clearly demonstrate quantum speed-up in this system, although the achieved success probability is considerably lower than the theoretically possible value of 100 %. The reduced fidelity is mainly due to relaxation and decoherence of the qubit state during the running of the algorithm and to a very small degree due to errors in the pulse sequence and drifts in the measurement equipment.

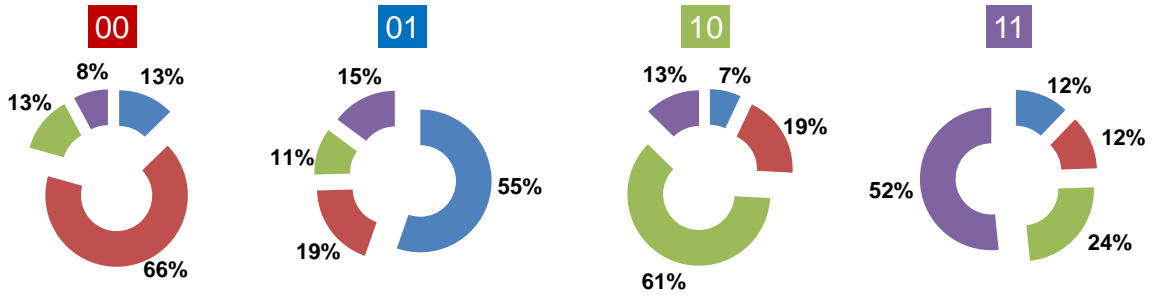


Figure 1.9: Single-run results when running the Grover search algorithm on our two-qubit quantum processor. Shown are the probabilities of obtaining the results 00, 01, 10, 11 as a function of the oracle function provided to the algorithm, indicated by the number on top of each graph. In all four cases, the success probability of the algorithm is $> 50\%$, thus outperforming any classical algorithm in the number of calls to the oracle function.

1.8 Designing a Scalable Quantum Computing Architecture

After having demonstrated the different building blocks of a superconducting, Transmon-based quantum processor it remains to be shown that larger-scale quantum-computing beyond two qubits is possible with this system. This work therefore pursued the realization of a more scalable qubit architecture using systems of up to six qubits coupled through a so-called “quantum bus” (Majer et al., 2007). The details of this novel architecture are discussed in the following sections.

The approach for scalable quantum computing with superconducting qubits pursued in this work consists of a system of many individual Transmon qubits equipped with individual JBA-based readouts, a multiplexed drive and readout circuit and a fixed qubit-qubit coupling mediated through a high-Q CPW resonator. As before, each qubit possesses a fluxline for fast frequency control. The readout and drive signals are sent to all the qubits in parallel through a multiplexed transmission line. In this approach, the qubit and readout parameters, couplings and frequencies have to be carefully to avoid unwanted coupling between individual qubits and readouts and to allow the implementation of robust quantum gates between individual qubits. In this work we realized a 4-qubit chip and characterized it experimentally. The results of these experiments will be discussed in the main text of this thesis.

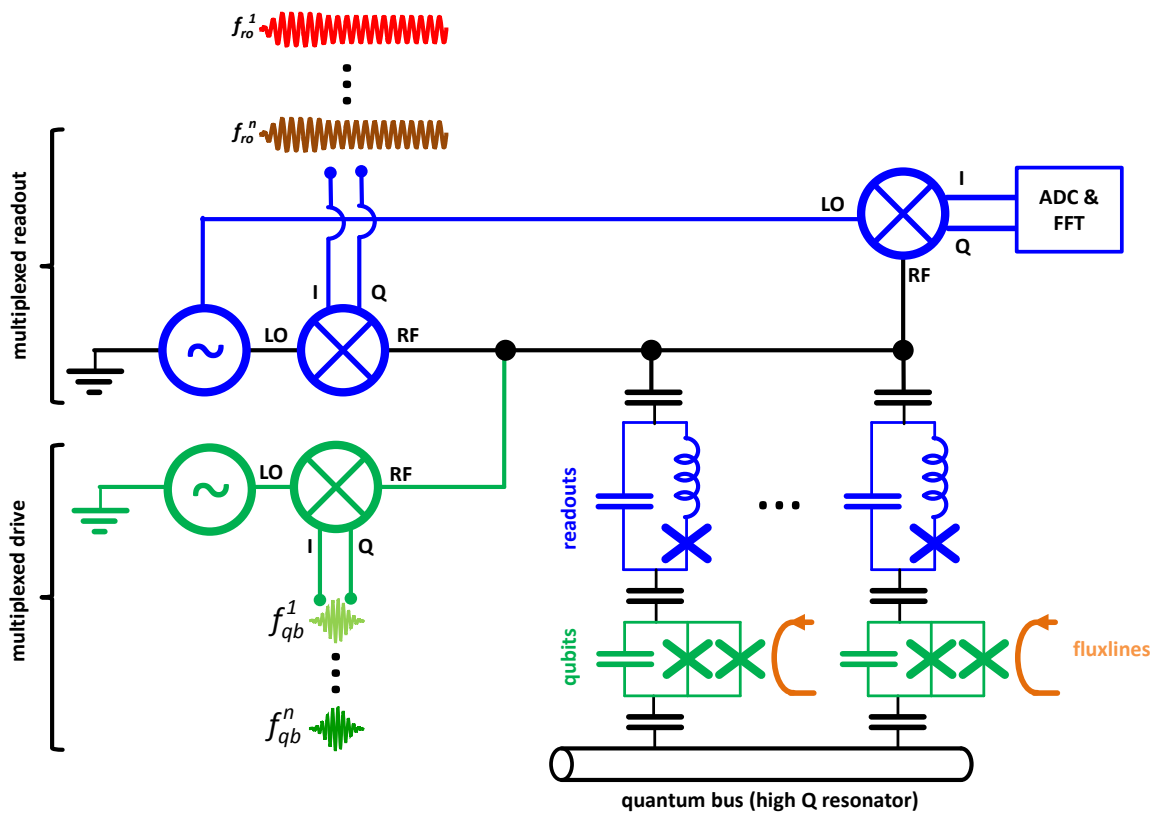


Figure 1.10: ...

Chapter 2

Theoretical Foundations

The goal of this chapter is to provide the theoretical foundations needed to interpret and analyze the experiments discussed in the following chapters. We will therefore briefly introduce some basic concepts of quantum mechanics and quantum computing, discuss Transmon qubits and circuit quantum electrodynamics (CQED) and introduce the reader to the Josephson bifurcation amplifier that we use to read out the qubit state in our experiments. Further details on all the elements discussed here will be provided in the relevant sections of the “Experiments” chapter.

2.1 Quantum mechanics & Quantum Computing

2.2 Transmon qubits

A Transmon qubit is essentially a Cooper pair box (CPB) operated in the phase regime, where $E_J \gg E_C$. The Hamiltonian of the CPB can be written as (Cottet, 2002)

$$\hat{H} = 4E_C (\hat{n} - n_g)^2 - E_J \cos \hat{\phi} \quad (2.1)$$

where $E_C = e^2/C_\Sigma$ is the charging energy with $C_\Sigma = C_J + C_B + C_g$ the total gate capacitance of the system, \hat{n} is the number of Cooper pairs transferred between the islands, n_g the gate charge, E_J the Josephson energy of the junction and $\hat{\phi}$ the quantum phase across the junction.

This Hamiltonian can be solved exactly in the phase basis with the solutions being

given as (Koch et al., 2007; Cottet, 2002)

$$E_m(n_g) = E_C a_{2[n_g + k(m, n_g)]}(-E_J/E_C) \quad (2.2)$$

Here, $a_\nu(q)$ denotes Mathieu's characteristic value and $k(m, n_g)$ is a function that sorts the eigenvalues. We'll denote the energy differences between individual eigenstates by $E_{ij} = E_j - E_i$. The absolute anharmonicity of the first two Transmon transitions is given as $\alpha \equiv E_{12} - E_{01}$, the relative anharmonicity as $\alpha_r \equiv \alpha/E_{01}$. In the limit $E_J \gg E_C$ these are well approximated by $\alpha \simeq -E_C$ and $\alpha_r \simeq -(8E_J/E_C)^{-1/2}$.

2.3 Circuit quantum electrodynamics

For readout and noise protection, the Transmon qubit is usually coupled to a harmonic oscillator which is usually realized as a lumped-elements resonator or a coplanar waveguide resonator. In the limit where the resonator capacity $C_r \gg C_\Sigma$ we can write the effective Hamiltonian of the system as

$$\hat{H} = \hbar \sum_j \omega_j |j\rangle \langle j| + \hbar \omega_r \hat{a}^\dagger \hat{a} + \hbar \sum_{i,j} g_{ij} |i\rangle \langle j| (\hat{a} + \hat{a}^\dagger) \quad (2.3)$$

Here, $\omega_r = 1/\sqrt{L_r C_r}$ gives the resonator frequency and \hat{a} (\hat{a}^\dagger) are annihilation (creation) operators acting on oscillator states. The voltage of the oscillator is given by $V_{rms}^0 = \sqrt{\hbar \omega_r / 2 C_r}$ and the parameter β gives the ratio between the gate capacitance and total capacitance, $\beta = C_g / C_\Sigma$. The coupling energies g_{ij} are given as

$$\hbar g_{ij} = 2\beta e V_{rms}^0 \langle i | \hat{n} | j \rangle = \hbar g_{ji}^* \quad (2.4)$$

When the coupling between the resonator and the Transmon is weak $g_{ij} \ll \omega_r, E_{01}/\hbar$ we can ignore the terms in eq. (2.3) that describe simultaneous excitation or deexcitation of the Transmon and the resonator and obtain a simpler Hamiltonian in the so-called *rotating wave approximation* given as

$$\hat{H} = \hbar \sum_j \omega_j |j\rangle \langle j| + \hbar \omega_r \hat{a}^\dagger \hat{a} + \left(\hbar \sum_i g_{i,i+1} |i\rangle \langle i+1| \hat{a}^\dagger + H.c. \right) \quad (2.5)$$

2.3.1 Dispersive limit & qubit readout

When the qubit frequency is far detuned from the resonator frequency direct qubit-resonator transition get exponentially suppressed and the only interaction left between the two system is a dispersive shift of the transition frequencies. In this limit, the effective Hamiltonian of the system can be written as (Blais et al., 2004; Koch et al., 2007)

$$\hat{H}_{eff} = \frac{\hbar\omega'_{01}}{2}\hat{\sigma}_z + \hbar(\omega'_r + \chi\hat{\sigma}_z)\hat{a}^\dagger\hat{a} \quad (2.6)$$

Here, the resonance frequencies of both the qubit and the resonator are shifted and given as $\omega'_r = \omega_r - \chi_{12}/2$ and $\omega'_{01} = \omega_{01} + \chi_{01}$. The dispersive shift χ itself is given as

$$\chi = \chi_{01} - \chi_{12}/2 \quad (2.7)$$

$$\chi_{ij} = \frac{g_{ij}^2}{\omega_{ij} - \omega_r} = \frac{(2\beta e V_{rms}^0)^2}{\hbar^2 \Delta_i} |\langle i | \hat{n} | i + 1 \rangle|^2 \quad (2.8)$$

The fact that χ_{01} and χ_{12} contribute to the total dispersive shift can cause the overall dispersive shift to become negative and even diverge at some particular working points.

2.4 The Josephson bifurcation amplifier

(Palacios-Laloy, 2010)

$$[L_e + L_J(i)]\ddot{q} + R_e\dot{q} + \frac{q}{C_e} = V_e \cos(\omega_m t) \quad (2.9)$$

Expanding this to second order in L_J leads to the expression

$$\left(L_e + L_J \left[1 + \frac{\dot{q}^2}{2I_0^2} \right] \right) \ddot{q} + R_e\dot{q} + \frac{q}{C_e} = V_e \cos(\omega_m t) \quad (2.10)$$

Defining the total inductance $L_t = L_e + L_J$, the participation ratio $p = L_J/L_t$, the resonance frequency $\omega_r = 1/\sqrt{L_t C_e}$ and the quality factor $Q = \omega_r L_t / R_e$ we can rewrite this as

$$\ddot{q} + \frac{\omega_r}{Q}\dot{q} + \omega_r^2 q + \frac{p\dot{q}^2\ddot{q}}{2I_0} = \frac{V_e}{L_t} \cos(\omega_m t) \quad (2.11)$$

Chapter 3

Realizing a Two-Qubit Processor

This chapter discusses the main experimental results of this thesis. We start by discussing the implementation of a superconducting two-qubit processor, discussing the characteristics of the Transmon qubits used in the processor, the readout scheme, single-qubit manipulation, two-qubit gates as well as the experimental procedures used for quantum state and quantum process tomography. The last section of this chapter will discuss the implementation of a quantum algorithm – so called Grover search algorithm – using our two-qubit processor and the demonstration of quantum speed-up achieved with our system.

3.1 Introduction & Motivation

As discussed in the introduction, the most simple, usable quantum processor contains two qubits that are coupled by an universal two-qubit gate and which in addition can be manipulated and read out individually. We realized such a two-qubit processor using two Transmon qubits, coupled through a fixed capacitance and readout out by individual single-shot readout of the JBA type. The circuit diagram of our processor is shown in fig. 3.1, showing the qubits, the drive and readout circuit and the coupling element between them. The following sections we'll discuss the parameters of individual parts of the processor.

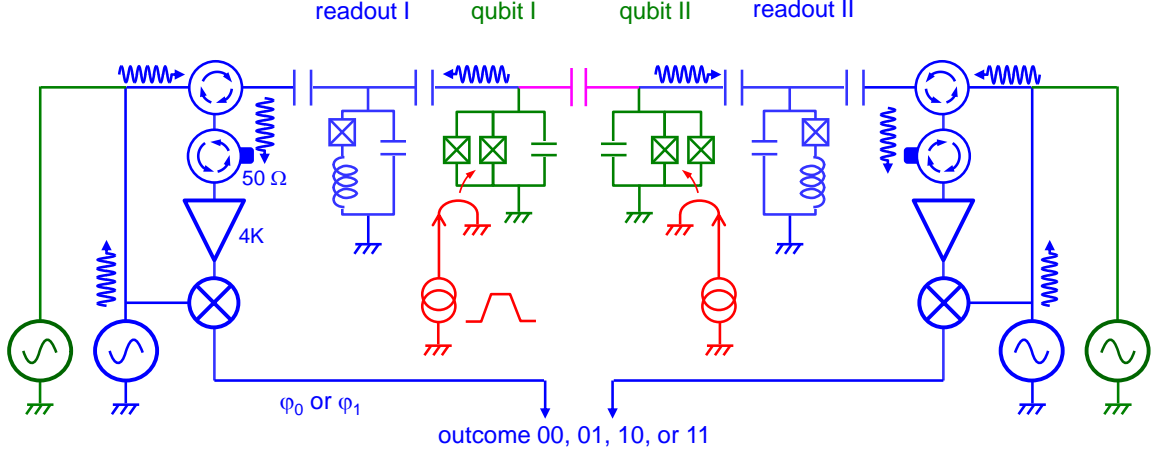


Figure 3.1: The circuit schematic of the two-qubit processor used in this work. Shown are the two Transmon qubits in green, the drive and readout circuit in blue, the fast flux lines in red and the coupling capacitance in magenta.

3.2 Processor Design

The parameters of the sample have been chosen in accordance to various design constraints of the qubit processor. For the qubits, the main design goals were high coherence time, good frequency tunability and fast drivability. As we will show later, the coherence time of the qubit is limited by relaxation to the ground state and coupling to external noise sources. The relaxation component of the Transmon qubit is ultimately limited by internal losses of the Josephson junction but usually is bound by coupling to the electromagnetic environment, as will be discussed later. The frequency tunability is important for the realization of fast two-qubit gates but can also limit the relaxation and coherence time of the qubit by coupling to external noise sources. The drivability speed on the other hand is limited by the anharmonicity of the qubit, which can however not be increased arbitrarily since it will make the qubit sensitive to charge noise when chosen too high. For the readout, the main design goals were readout speed and fidelity. The speed of the readout is limited by the quality factor of the readout resonator, which however also can induce qubit relaxation through the Purcell effect and may therefore not be chosen too small.

In the following paragraphs we'll therefore discuss the parameter design for our two-qubit processor and analyze the sample parameters that have been obtained.

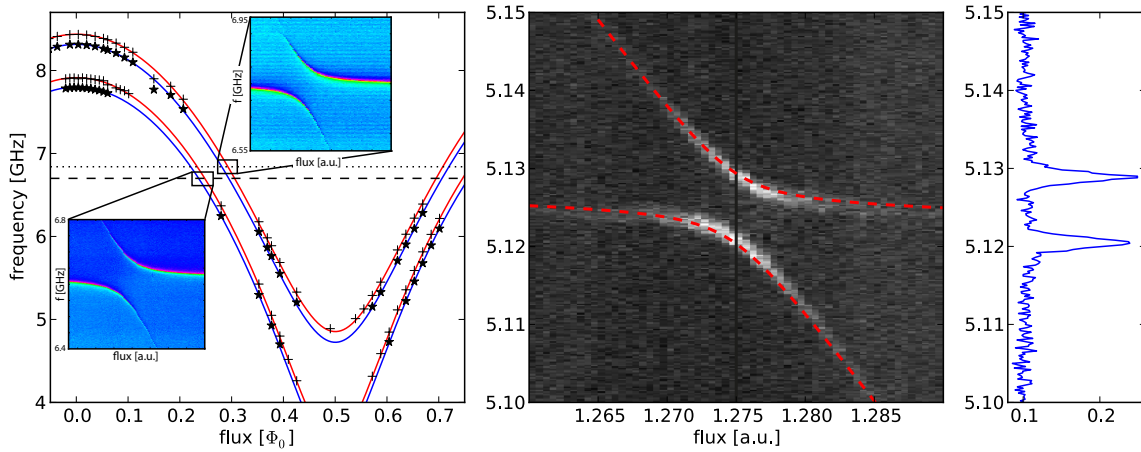


Figure 3.2: Spectroscopy of the realized two-qubit processor. a) $|0\rangle \rightarrow |1\rangle$ and $(|0\rangle \rightarrow |2\rangle)/2$ transition frequencies of the two qubits with fitted dependence and cavity frequencies. b) Avoided level crossing of the $|01\rangle$ and $|10\rangle$ levels of the qubits with fit, $g = 8.7$ MHz. c) Spectroscopy of qubit 1 at the point indicated in b).

3.3 Processor Fabrication

In this section we will discuss the fabrication of the two-qubit processor realized in this work.

Chapter 4

Measurement Setup & Techniques

Fig. 4.1 show the measurement setup used for the two-qubit experiments. We use the following components along the measurement chain to generate, mix and read out microwave and DC signals:

- *Qubit microwave pulses:* We use two continuous-wave microwave generators that generate phase-locked single-frequency microwave tones which are used for driving the two qubits. These pulses are mixed with fast control pulses generated by an arbitrary waveform generators (Tektronix AWG5014b) using a passive Hittite IQ mixer. By using sideband mixing in the frequency range of 0-300 MHz we can generate multi-frequency drive pulses with arbitrary frequency and phase shift in respect to the drive tone. The IQ mixer exhibits frequency-dependent amplitude and phase errors which are measured using a fast spectrum analyzer (Rhode & Schwarz FSP series) and corrected by adapting the AWG waveform fed to the mixer (see Appendix).
- *Flux pulses:* We use a second pair of AWGs to generate the flux drive pulses of each qubit. These pulses are attenuated by 20 dB and filtered using both conventional microwave low-pass filters as well as a pair of absorptive custom-made Eccosorb microwave filters, which exhibit a very high attenuation up to UHF frequencies (see Appendix for more details) [!9!](#) . The flux signal is fed back to room temperature through an identical piece of transmission line, which permits the measurement and compensation of the signal distortion caused by the response function of the transmission line (see Appendix for more details) [!10!](#) .

To Do 9: add exact link!

To Do 10: add exact link!

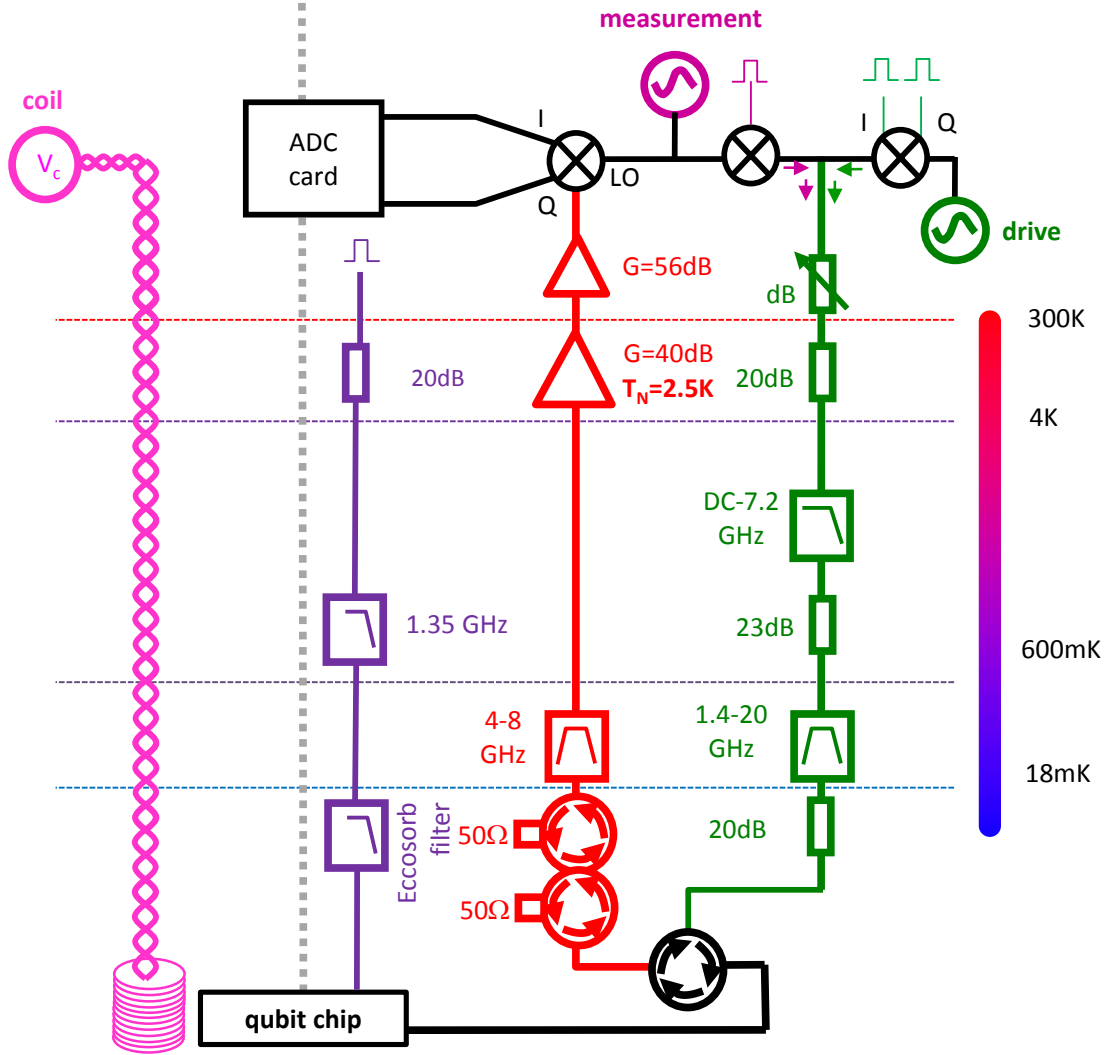


Figure 4.1: The measurement setup used for the two-qubit experiments. Exactly the same drive and readout scheme is used for both qubits with phase-locked microwave sources and arbitrary waveform generators.

- **Readout pulses:** We use a pair of continuous-wave microwave generators (Anritsu MG3692B) to generate a single-frequency pump tone which is mixed with a pulse shape signal generated by an arbitrary function generator (Tektronix AFG6352), fed through a tunable attenuator and combined with the qubit drive pulses. The readout pulses typically possess a rise time of 30 ns, a hold time of 200 ns and a latch time of about 2 μs at 90 % of the hold height.

- *Drive and measurement line*: The combined drive and readout signals are attenuated by 70 dB on their way to the qubit chip, where they are reflected and sent back through an output line connected to the input by a cryogenic circulator (PAMTECH **!11!**). The reflected measurement signal gets bandpass-filtered and amplified by a cryogenic HEMT amplifier and several room-temperature amplifiers. At room temperature it gets IQ-demodulated with the original continuous microwave tone and digitized by a four-channel 4GS/s ADC card (Acqiris DC282).

To Do 11: add the exact reference here

4.1 Measurement techniques

In this section we will discuss the techniques used to characterize and manipulate our two-qubit processor. All techniques employed are based on ...

Chapter 5

Processor Characterization

This section discusses the detailed characterization of individual circuit parts that will be used later to realize two-qubit gate and to run a quantum algorithm on the processor. The discussion will focus on the readout and microwave manipulation of the qubits as well as on the reconstruction of quantum states from measurement data, which will be used later for characterizing gate and processor operation.

5.0.1 Spectroscopic measurements

The following section discusses the parameters of our two-qubit processor that have been obtained by various measurements.

Qubit Parameters

Readout Parameters

- *Qubits*: Spectroscopic measurement of the qubit transitions yielded parameter values of $E_J^I/h = 36.2$ GHz, $E_c^I/h = 0.98$ GHz and $E_J^{II}/h = 43.1$ GHz, $E_c^{II}/h = 0.87$ GHz for the Josephson and charging energies of the two qubits and values of $d^I = 0.2$, $d^{II} = 0.35$ for the qubit junction asymmetries.
- *Readout resonator*: The frequencies of the readout resonators have been measured as $\nu_R^I = 6.84$ GHz and $\nu_R^{II} = 6.70$ GHz with quality factors $Q^I \simeq Q^{II} = 730$, independent measurements of the Kerr nonlinearities yielded $K^I/\nu_R^I \simeq K^{II}/\nu_R^{II} = -2.3 \pm 0.5 \times 10^{-5}$!12! .

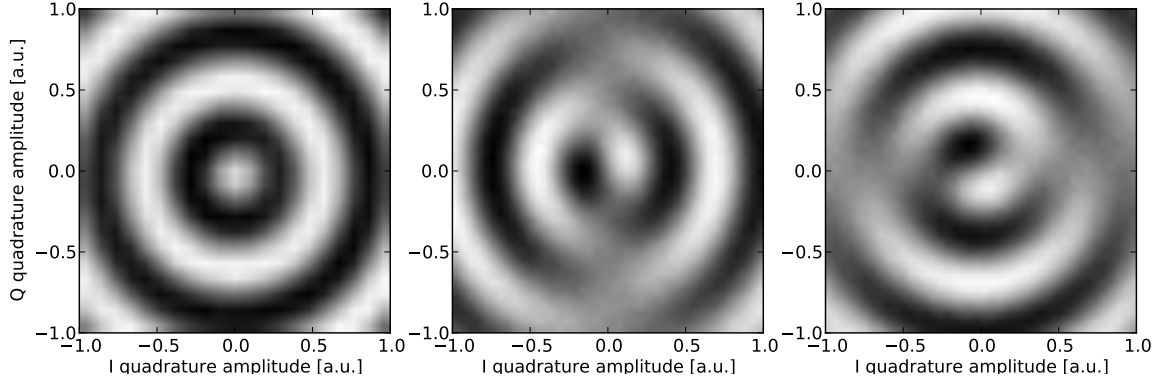


Figure 5.1

- *Qubit-Resonator coupling*: The coupling of the qubits to the readout resonators has been spectroscopically determined as $g_0^I \simeq g_0^{II} = 50$ MHz

5.0.2 Readout

5.0.3 Single-Qubit Operations

5.0.4 Quantum State Tomography

Quantum state tomography is the procedure of experimentally determining an unknown quantum state (Michael A. Nielsen and Isaac L. Chuang, 2000).

The density matrix of an n -qubit system can be written in general form as

$$\rho = \sum_{v_1, v_2, \dots, v_n} \frac{c_{v_1, v_2, \dots, v_n} \sigma_{v_1} \otimes \sigma_{v_2} \dots \sigma_{v_n}}{2^n} \quad (5.1)$$

$$c_{v_1, v_2, \dots, v_n} = \text{tr}(\sigma_{v_1} \otimes \sigma_{v_2} \dots \otimes \sigma_{v_n} \rho) \quad (5.2)$$

where $v_i \in \{X, Y, Z, I\}$ and n gives the number of qubits in the system and where the c_{v_1, v_2, \dots, v_n} are real-valued coefficients that fully describe the given density matrix. To reconstruct the density matrix of an experimental quantum system in a well-prepared state it is therefore sufficient to measure the expectation values of these $n^2 - 1$ coefficients on an ensemble of identically prepared systems. However, statistical and systematic measurement errors can yield a set of coefficients that corresponds to a *non-physical*

density matrix which violates either the positivity or unity-trace requirement. In the following paragraph we will therefore discuss a technique with which one can estimate the density matrix of a system in a more correct way.

Maximum Likelihood Estimation

A method which is often used in quantum state tomography is the so-called *maximum-likelihood* technique. Rather than directly calculating the density matrix of the system from the obtained expectation values $c_{v_1, v_2 \dots v_n}$, it calculates the joint probability of measuring a set $\{c_{X,X,\dots,X}, c_{Y,X,\dots,X}, \dots, c_{I,I,\dots,I}\}$ for a given estimate of the density matrix $\hat{\rho}$. By numerically or analytically maximizing this joint probability over the set of possible density matrices we obtain the density matrix which is most likely to have produced the set of measurement outcomes that we have observed.

The joint measurement operators $\Sigma_j = \sigma_{v_1} \otimes \sigma_{v_2} \dots \otimes \sigma_{v_n}$ have the eigenvalues ± 1 and can thus be written as

$$\sigma_{v_1} \otimes \sigma_{v_2} \dots \otimes \sigma_{v_n} = |+_j\rangle \langle +_j| - |-_j\rangle \langle -_j| \quad (5.3)$$

where $|+_j\rangle$ and $|-_j\rangle$ are the eigenstates corresponding to the eigenvalues ± 1 of Σ_j . The expectation value $\langle \Sigma_j \rangle$ can be estimated by the quantity

$$\widehat{\langle \Sigma_j \rangle}_\rho = \frac{1}{l} \sum_{i=1}^l M_i(\Sigma_j, \rho) \quad (5.4)$$

where $M_i(M, \rho)$ denotes the outcome of the i -th measurement of the operator M on the state described by the density matrix ρ . This quantity is binomially distributed with the expectation value $E(\widehat{\langle \Sigma_j \rangle}_\rho) = \langle \Sigma_j \rangle_\rho$ and the variance $\sigma^2(\widehat{\langle \Sigma_j \rangle}_\rho) = 1/l \cdot (1 - \langle \Sigma_j \rangle_\rho^2)$. For large sample sizes l , the binomial distribution can be well approximated by a normal distribution with the same expectation value and variance. The joint probability of obtaining a set of measurement values $\{s_1, \dots, s_{n^2-1}\}$ for the set of operators $\{\widehat{\langle \Sigma_1 \rangle}_\rho, \dots, \widehat{\langle \Sigma_{n^2-1} \rangle}_\rho\}$ is then given as

$$P\left(\widehat{\langle \Sigma_1 \rangle}_\rho = s_1; \dots; \widehat{\langle \Sigma_{n^2-1} \rangle}_\rho = s_{n^2-1}\right) = \prod_{i=1}^{n^2-1} \exp\left(-\frac{l}{2} \frac{(s_i - \langle \Sigma_i \rangle_\rho)^2}{1 - \langle \Sigma_i \rangle_\rho^2}\right) \quad (5.5)$$

By maximizing this probability (or the logarithm of it) we obtain an estimate of the density

matrix ρ of the quantum state. This technique also allows us to include further optimization parameters when calculating the joint probability. This is useful for modeling e.g. systematic errors of the measurement or preparation process, which can be described by modifying the operators contained in the probability sum. A common source of errors in our tomography measurements are errors in the microwave pulses used to drive the qubit. Since our measurement apparatus permits us only to measure the σ_z operator of each qubit we have to perform $\pi/2$ rotations about the Y or $-X$ axes of the Bloch sphere of each individual qubit in order to measure the values of the σ_x and σ_y operators, which we therefore replace with an effective measurement of each qubits σ_z operator preceded by a rotation R_{ν_i} given as

$$R_X = \exp(-i\sigma_y\pi/4) \quad (5.6)$$

$$R_Y = \exp(+i\sigma_x\pi/4) \quad (5.7)$$

Phase and amplitude errors can be modeled as

$$R_X = \exp(-i[+\sigma_y \cos \alpha + \sigma_x \sin \alpha][\pi/4 + \gamma]) \quad (5.8)$$

$$R_Y = \exp(+i[-\sigma_y \sin \beta + \sigma_x \cos \beta][\pi/4 + \delta]) \quad (5.9)$$

Here, α and β represent phase errors whereas γ and δ represent amplitude errors in the drive pulses.

5.0.5 Two Qubit Operations

Creation of Entanglement

Violation of Bell's inequality

5.0.6 Characterizing Quantum Processes

Introduction & Principle

Implementation

A quantum process can be described as a map $\mathcal{E} : \rho_{\mathcal{H}} \rightarrow \rho_{\mathcal{H}}$ that maps a density matrix ρ defined in a Hilbert space Q_1 to another density matrix $\mathcal{E}(\rho)$ defined in a target

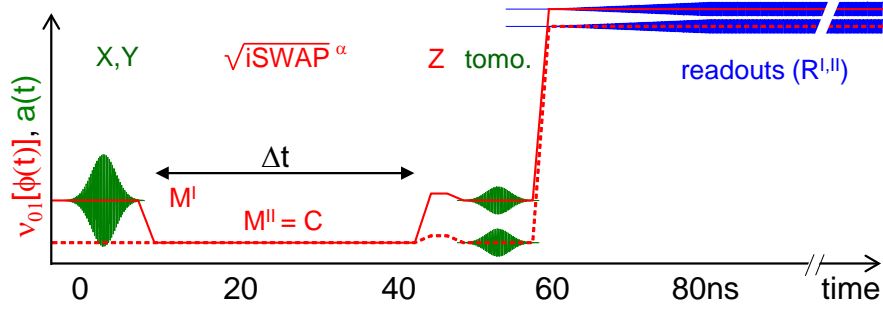


Figure 5.2

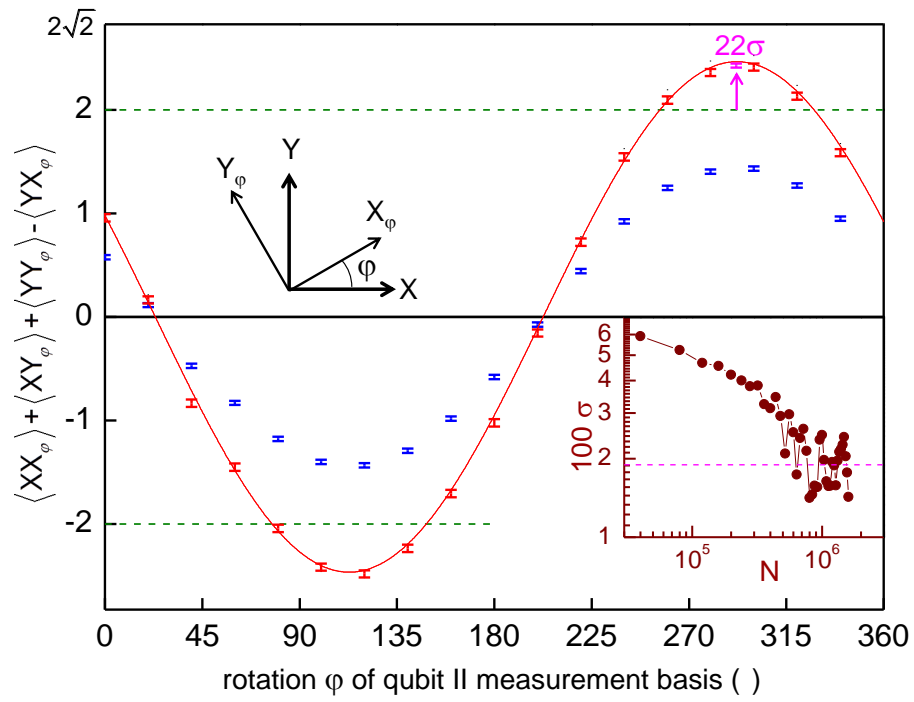


Figure 5.3

Hilbert space Q_2 and fulfilling three axiomatic properties Michael A. Nielsen and Isaac L. Chuang (2000); Haroche and Raimond (2006):

Axiom 5.0.1. $\text{tr}[\mathcal{E}(\rho)]$ is the probability that the process represented by \mathcal{E} occurs, when ρ is the initial state.

Axiom 5.0.2. \mathcal{E} is a *convex-linear map* on the set of density matrices, that is, for probabilities $\{p_i\}$,

$$\mathcal{E}\left(\sum_i p_i \rho_i\right) = \sum_i p_i \mathcal{E}(\rho_i) \quad (5.10)$$

Axiom 5.0.3. \mathcal{E} is a *completely-positive* map. That is, if \mathcal{E} maps density operators of system Q_1 to density operators of system Q_2 , then $\mathcal{E}(A)$ must be positive for any positive operator A . Furthermore, if we introduce an extra system R of arbitrary dimensionality, it must be true that $(\mathcal{I} \otimes \mathcal{E})(A)$ is positive for any positive operator A on the combined system RQ_1 , where \mathcal{I} denotes the identity map on system R .

As shown in Michael A. Nielsen and Isaac L. Chuang (2000), any quantum process fulfilling these criteria can be written in the form

$$\mathcal{E}(\rho) = \sum_i E_i \rho E_i^\dagger \quad (5.11)$$

for some set of operators $\{E_i\}$ which map the input Hilbert space to the output Hilbert space, and $\sum_i E_i^\dagger E_i \leq I$.

Now, if we express the operators E_i in a different operator basis \tilde{E}_j such that $E_i = \sum_j a_{ij} \tilde{E}_j$ and insert into eq. (5.11), we obtain

$$\mathcal{E}(\rho) = \sum_i \sum_j a_{ij} \tilde{E}_j \rho \sum_k a_{ik}^* \tilde{E}_k^\dagger \quad (5.12)$$

$$= \sum_{j,k} \tilde{E}_j \rho \tilde{E}_k^\dagger \sum_i a_{ij} a_{ik}^* \quad (5.13)$$

$$= \sum_{j,k} \tilde{E}_j \rho \tilde{E}_k^\dagger \chi_{jk} \quad (5.14)$$

where we defined $\chi_{jk} = \sum_i a_{ij} a_{ik}^*$. This is the so-called χ -matrix representation of the quantum process. Here, all the information on the process is contained in the χ matrix,

which controls the action of the process-independent operators \tilde{E}_i on the initial density matrix ρ .

Now, the goal of *quantum process tomography* is to obtain the coefficients of the χ -matrix – or any other complete representation of the process – from a set of experimentally measured density matrices ρ and $\mathcal{E}(\rho)$.

To achieve this, several techniques have been developed. The technique used in this work is the so-called *standard quantum process tomography (SQPT)*. This technique proceeds as follows:

1. Choose a set of operators E_i that forms a full basis of $\mathcal{M} : Q_1 \rightarrow Q_2$. For n-qubit process tomography we usually choose $E_{i_1, i_2 \dots i_n} = \sigma_{i_1} \otimes \sigma_{i_2} \dots \otimes \sigma_{i_n}$, where σ_i are the single-qubit Pauli operators and $i \in \{I, X, Y, Z\}$.
2. Choose a set of pure quantum states $|\phi_i\rangle$ such that $|\phi_i\rangle \langle \phi_i|$ span the whole space of input density matrices ρ . Usually, for a n-qubit system we choose $\phi = \{|0\rangle, |1\rangle, (|0\rangle + |1\rangle)/\sqrt{2}, (|0\rangle + i|1\rangle)/\sqrt{2}\}^{\otimes n}$, where $^{\otimes n}$ denotes the n-dimensional Kronecker product of all possible permutations.
3. For each of the $|\phi_i\rangle$, determine $\mathcal{E}(|\phi_i\rangle \langle \phi_i|)$ by quantum state tomography. Usually we also determine $|\phi_i\rangle \langle \phi_i|$ experimentally since the preparation of this state already entails small preparation errors that should be taken into account when performing quantum process tomography.

After having obtained the ρ_i and $\mathcal{E}(\rho_i)$ one obtains the χ -matrix by writing $\mathcal{E}(\rho_i) = \sum_j \lambda_{ij} \tilde{\rho}_j$, with some arbitrary basis $\tilde{\rho}_j$ and letting $\tilde{E}_m \tilde{\rho}_j \tilde{E}_n^\dagger = \sum_k \beta_{jk}^{mn} \tilde{\rho}_k$. We can then insert into eq. (5.14) and obtain

$$\sum_k \lambda_{ik} \tilde{\rho}_k = \sum_{m,n} \chi_{mn} \sum_k \beta_{ik}^{mn} \tilde{\rho}_k \quad (5.15)$$

This directly yields $\lambda_{ik} = \sum_{m,n} \beta_{ik}^{mn} \chi_{mn}$, which, by linear inversion, gives χ .

The Kraus representation

Besides the χ -matrix representation, there is another useful way of expressing a quantum map, the so called *Kraus representation*, which is given as

$$\mathcal{E}(\rho) = \sum_i M_i \rho M_i^\dagger \quad (5.16)$$

It can be shown (Haroche and Raimond, 2006) that this sum contains at most N elements, where N is the dimension of the Hilbert space of the density matrix ρ . We can go from the χ representation to the Kraus representation by changing the basis \tilde{E}_i such that

$$\tilde{E}_i = \sum_l a_{il} \check{E}_l \quad (5.17)$$

which, for eq. (5.14), yields

$$\mathcal{E}(\rho) = \sum_{j,k} \sum_l a_{jl} \check{E}_l \rho \sum_m a_{km}^* \check{E}_m^\dagger \chi_{jk} \quad (5.18)$$

$$= \sum_{l,m} \check{E}_l \rho \check{E}_m^\dagger \sum_{j,k} a_{jl} a_{km}^* \chi_{jk} \quad (5.19)$$

The last sum on the right side of eq. (5.19) corresponds to a change of coordinates of the matrix χ . Now, we can pick the a such that χ is diagonal in the new basis \check{E} and obtain

$$\mathcal{E}(\rho) = \sum_l \lambda_l \check{E}_l \rho \check{E}_l^\dagger \quad (5.20)$$

$$= \sum_l M_l \rho M_l^\dagger \quad (5.21)$$

with λ_l being the l -th eigenvalue of the χ matrix with the eigen-operator \check{E}_l and $M_l = \sqrt{\lambda_l} \check{E}_l$.

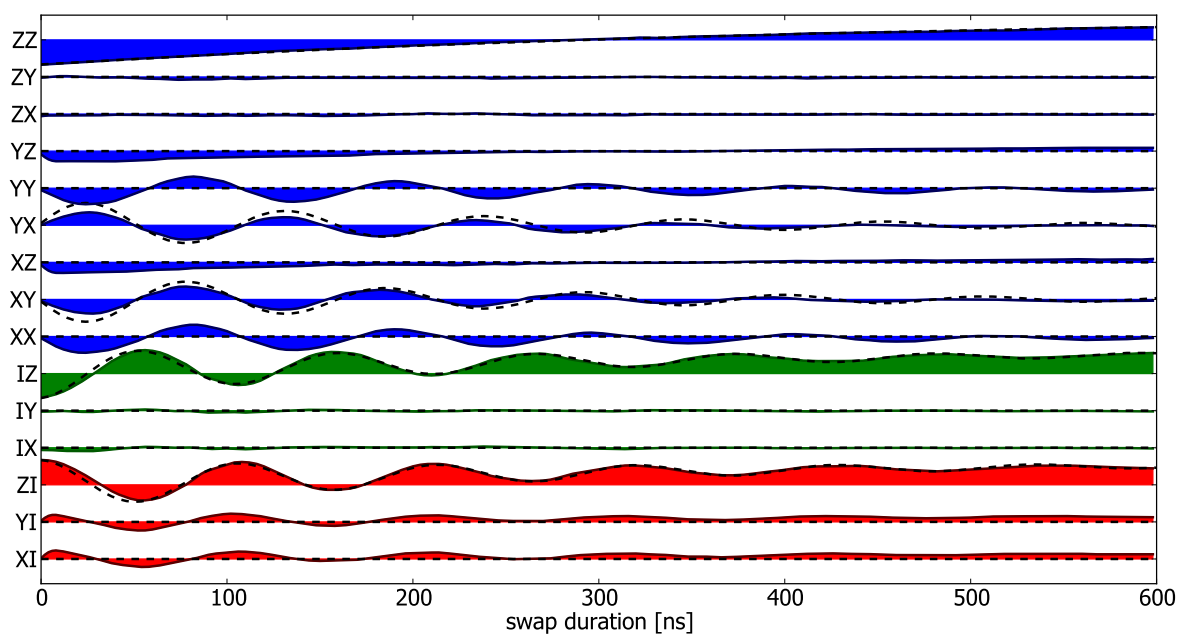


Figure 5.4: testcaption

5.0.7 Realizing a Two-Qubit Gate

Principle

Implementation

Fidelity

Error Analysis

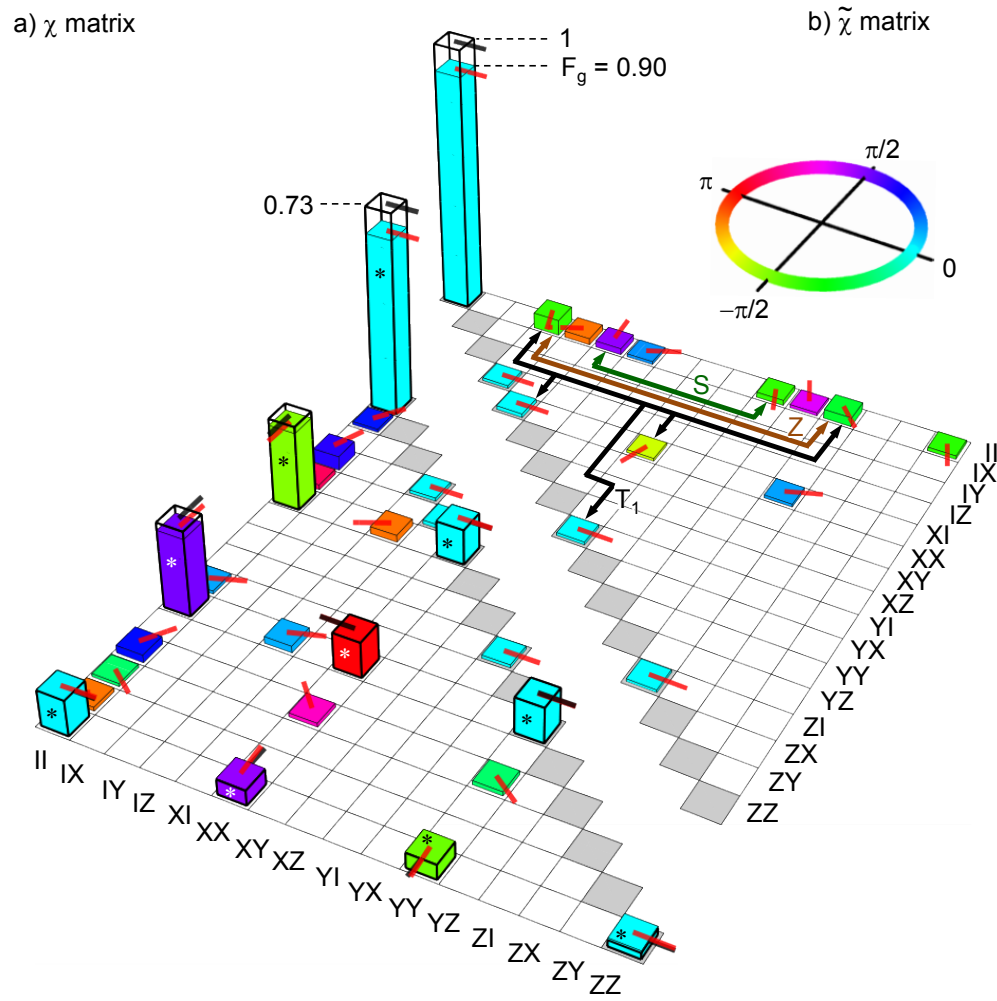


Figure 5.5

Chapter 6

Running the Grover Search Algorithm

6.0.8 Introduction & Motivation

1. Inputs: An oracle function \mathcal{O} which performs the operation $\mathcal{O} |x\rangle |q\rangle = |x\rangle |q \otimes f(x)\rangle$, where $f(x) = \delta_{x,x_0}$
2. Outputs: The marked state x_0
3. Initialize the qubit register to the state:

$$|\psi\rangle \rightarrow |0\rangle^{\otimes n} |0\rangle$$

4. Apply the Hadamard transformation to all of the qubits:

$$|psi\rangle \rightarrow \frac{1}{\sqrt{2^n}} \sum_{x=0}^{2^n-1} |x\rangle \left[\frac{|0\rangle - |1\rangle}{\sqrt{2}} \right]$$

5. Apply the Grover iteration $R \approx [\pi\sqrt{2^n}/4]$ times:

$$|\psi\rangle \rightarrow [(2|\psi\rangle\langle\psi| - I)\mathcal{O}]^R \frac{1}{\sqrt{2^n}} \sum_{x=0}^{2^n-1} |x\rangle \left[\frac{|0\rangle - |1\rangle}{\sqrt{2}} \right] \approx |x_0\rangle \left[\frac{|0\rangle - |1\rangle}{\sqrt{2}} \right]$$

6. Measure the first n qubits to obtain x_0

For the Two-qubit case, this algorithm can be drastically simplified – or “compiled” – such that it runs without the ancilla qubit and in one single step of the Grover iteration:

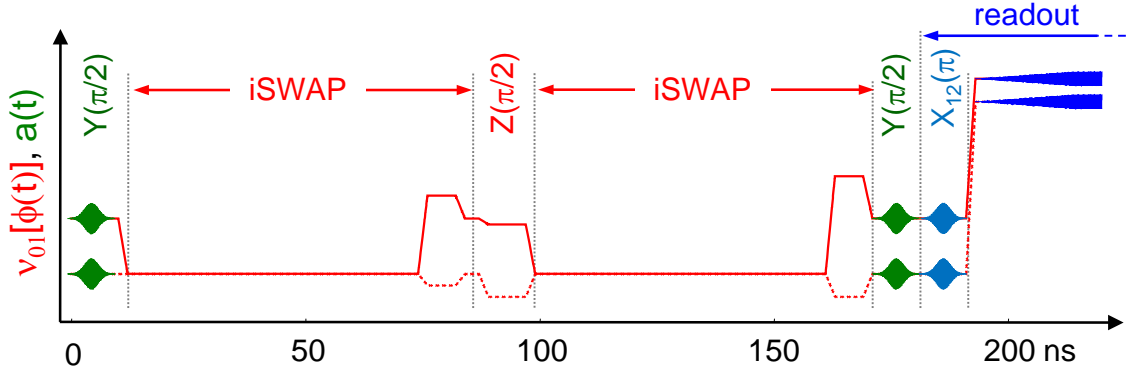


Figure 6.1: The pulse sequence used in realizing Grover's quantum search algorithm. First, a $Y_{\pi/2}$ pulse is applied to each qubit to produce the fully superposed state $1/2(|00\rangle + |01\rangle + |10\rangle + |11\rangle)$. Then, an i SWAP gate is applied, followed by a $Z_{\pm\pi/2}$ gate on each qubit, which corresponds to the application of the oracle function. The resulting state is then analyzed using another i SWAP gate and two $Y_{\pi/2}$ gates to extract the state which has been marked by the oracle function. Optionally, a Y_{π}^{12} pulse is used on each qubit to increase the readout fidelity.

1. **Inputs:** An oracle function \mathcal{O} which performs the operation $\mathcal{O}|x\rangle = (-1)^{\delta_{x,x_0}}|x\rangle$, where x_0 is the marked state that is searched.
2. **Outputs:** The marked state x_0
- 3.

6.0.9 Experimental Implementation

6.0.10 Results

Algorithm Fidelity

Single-Run Probabilities

Error Analysis

6.0.11 Conclusions

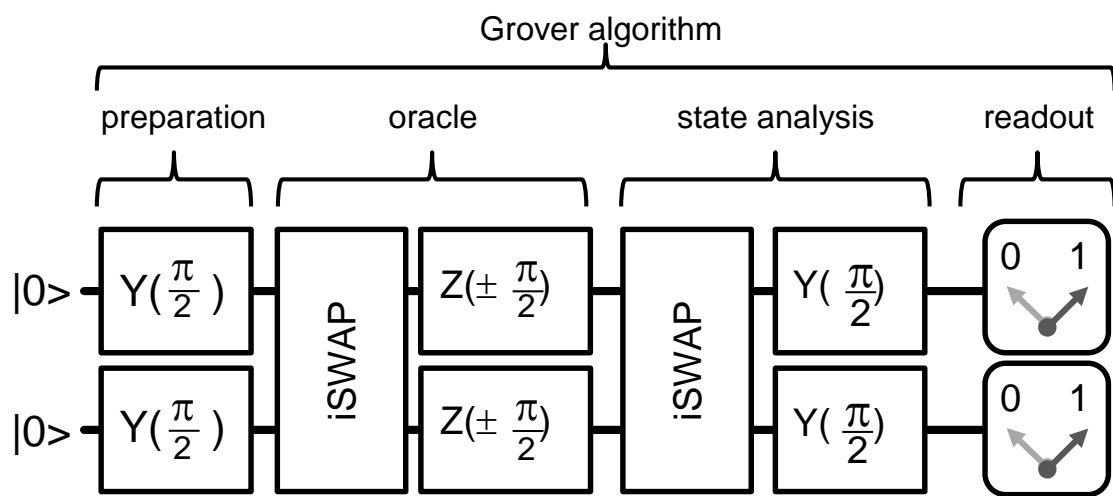


Figure 6.2

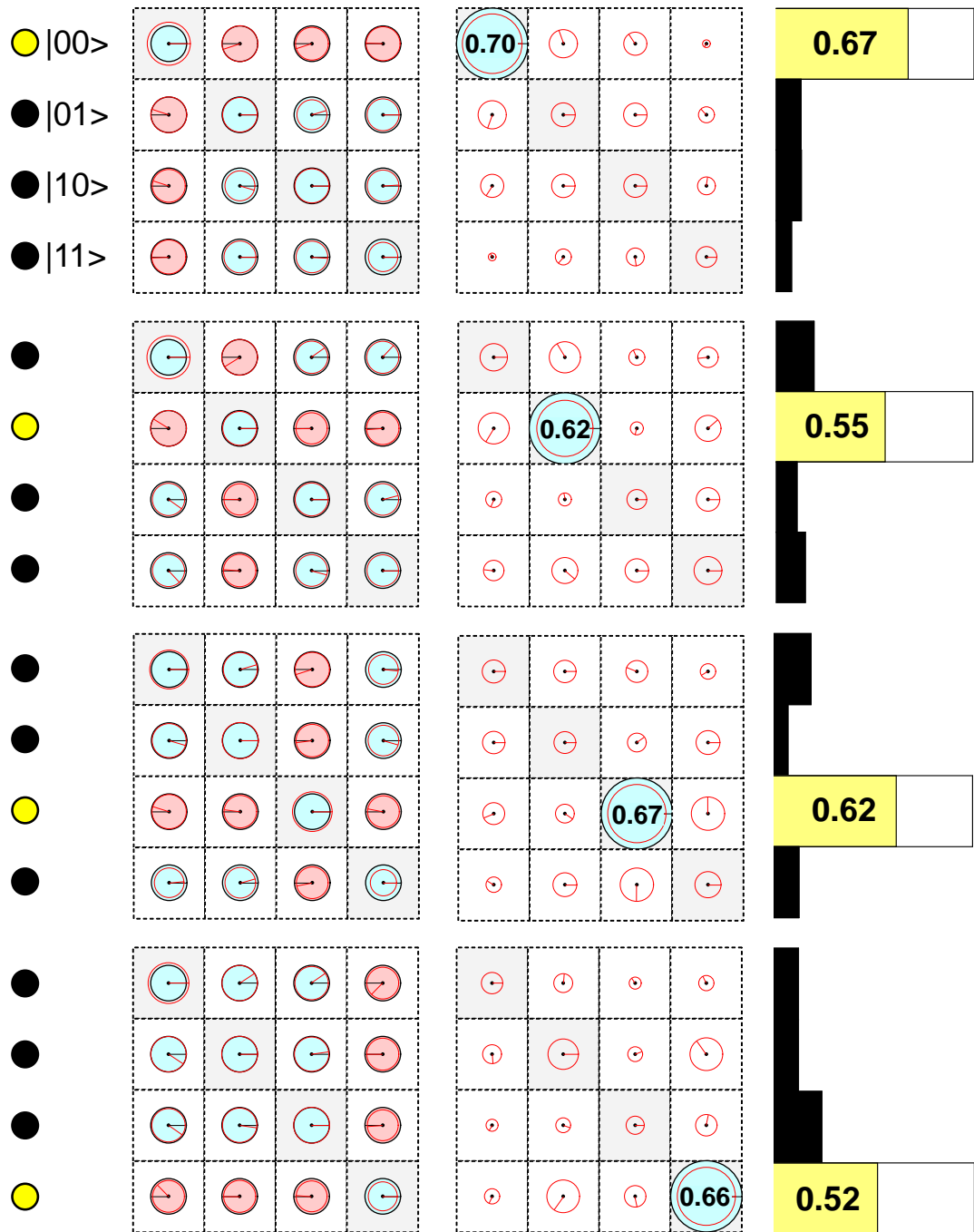


Figure 6.3

Chapter 7

Scalable Architectures for Quantum Bits

7.1 Definition & Requirements

7.2 Qubit Design

7.3 Microwave Driving

7.4 Frequency Manipulation

7.5 Readout

7.6 Coupling

7.7 A 4-Qubit Architecture

7.8 Scaling Up

Chapter 8

Conclusions & Outlook

8.1 Future Directions in Superconducting QC

8.1.1 3D Circuit Quantum Electrodynamics

8.1.2 Hybrid Quantum Systems

8.1.3 Quantum Error Correction & Feedback

Appendix A

Modeling of Multi-Qubit Systems

A.1 Analytical Approach

A.1.1 Multi-Qubit Hamiltonian

A.1.2 Energies and Eigenstates

A.2 Master Equation Approach

$$\frac{d\rho}{dt} = -\frac{i}{\hbar}[H, \rho] + \sum_j \left[2L_j \rho L_j^\dagger - \{L_j^\dagger L_j, \rho\} \right] \quad (\text{A.1})$$

A.2.1 Direct Integration

A.2.2 Monte Carlo Simulation

A.2.3 Speeding Up Simulations

Appendix B

Data Acquisition & Management

B.1 Data Acquisition Infrastructure

B.2 Data Management Requirements

B.3 PyView

B.3.1 Overview

B.3.2 Instrument Management

B.3.3 Data Acquisition

B.3.4 Data Management

B.3.5 Data Analysis

Appendix C

Design & Fabrication

C.1 Mask Design

C.2 Optical Lithography

C.3 Electron Beam Lithography

Bibliography

- Blais, A., Huang, R., Wallraff, A., Girvin, S. M., and Schoelkopf, R. J. (2004). Cavity quantum electrodynamics for superconducting electrical circuits: An architecture for quantum computation. *Physical Review A*, 69(6):062320.
- Chiorescu, I., Nakamura, Y., Harmans, C. J. P. M., and Mooij, J. E. (2003). Coherent quantum dynamics of a superconducting flux qubit. *Science*, 299(5614):1869–1871.
- Clauser, J. F., Horne, M. A., Shimony, A., and Holt, R. A. (1969). Proposed experiment to test local Hidden-Variable theories. *Physical Review Letters*, 23(15):880–884.
- Collin, E., Ithier, G., Aassime, A., Joyez, P., Vion, D., and Esteve, D. (2004). NMR-like control of a quantum bit superconducting circuit. *Physical Review Letters*, 93(15):157005.
- Cottet, A. (2002). *Implementation of a quantum bit in a superconducting circuit*. PhD thesis, Université Paris VI, Paris.
- DiCarlo, L., Chow, J. M., Gambetta, J. M., Bishop, L. S., Johnson, B. R., Schuster, D. I., Majer, J., Blais, A., Frunzio, L., Girvin, S. M., and Schoelkopf, R. J. (2009). Demonstration of two-qubit algorithms with a superconducting quantum processor. *Nature*, 460(7252):240–244.
- DiCarlo, L., Reed, M. D., Sun, L., Johnson, B. R., Chow, J. M., Gambetta, J. M., Frunzio, L., Girvin, S. M., Devoret, M. H., and Schoelkopf, R. J. (2010). Preparation and measurement of three-qubit entanglement in a superconducting circuit. *Nature*, 467(7315):574–578.
- DiVincenzo, D. P. (2000). The physical implementation of quantum computation. *Fortschritte der Physik*, 48(9-11):771–783.

- Grover, L. K. (1997). Quantum mechanics helps in searching for a needle in a haystack. *Physical Review Letters*, 79(2):325–328.
- Haroche, S. and Raimond, J. (2006). *Exploring the Quantum: Atoms, Cavities and Photons*. Oxford University Press.
- Koch, J., Yu, T. M., Gambetta, J., Houck, A. A., Schuster, D. I., Majer, J., Blais, A., Devoret, M. H., Girvin, S. M., and Schoelkopf, R. J. (2007). Charge-insensitive qubit design derived from the cooper pair box. *Physical Review A*, 76(4):042319.
- Majer, J., Chow, J. M., Gambetta, J. M., Koch, J., Johnson, B. R., Schreier, J. A., Frunzio, L., Schuster, D. I., Houck, A. A., Wallraff, A., Blais, A., Devoret, M. H., Girvin, S. M., and Schoelkopf, R. J. (2007). Coupling superconducting qubits via a cavity bus. *Nature*, 449(7161):443–447.
- Mallet, F., Ong, F. R., Palacios-Laloy, A., Nguyen, F., Bertet, P., Vion, D., and Esteve, D. (2009). Single-shot qubit readout in circuit quantum electrodynamics. *Nat Phys*, 5(11):791–795.
- Martinis, J. M., Devoret, M. H., and Clarke, J. (1985). Energy-Level quantization in the Zero-Voltage state of a Current-Biased josephson junction. *Physical Review Letters*, 55(15):1543–1546.
- Martinis, J. M., Nam, S., Aumentado, J., and Urbina, C. (2002). Rabi oscillations in a large Josephson-Junction qubit. *Physical Review Letters*, 89(11):117901.
- Michael A. Nielsen and Isaac L. Chuang (2000). *Quantum Computation and Quantum Information*. Cambridge University Press.
- Mooij, J. E., Orlando, T. P., Levitov, L., Tian, L., van der Wal, C. H., and Lloyd, S. (1999). Josephson Persistent-Current qubit. *Science*, 285(5430):1036 –1039.
- Nakamura, Y., Pashkin, Y. A., and Tsai, J. S. (1999). Coherent control of macroscopic quantum states in a single-Cooper-pair box. *Nature*, 398(6730):786–788.
- Paik, H., Schuster, D. I., Bishop, L. S., Kirchmair, G., Catelani, G., Sears, A. P., Johnson, B. R., Reagor, M. J., Frunzio, L., Glazman, L. I., Girvin, S. M., Devoret, M. H., and Schoelkopf, R. J. (2011). Observation of high coherence in josephson junction qubits

- measured in a Three-Dimensional circuit QED architecture. *Physical Review Letters*, 107(24):240501.
- Palacios-Laloy, A. (2010). *Superconducting qubit in a resonator: Test of the Leggett-Garg inequality and single-shot readout*. PhD thesis, Université Paris VI, Paris.
- Siddiqi, I., Vijay, R., Metcalfe, M., Boaknin, E., Frunzio, L., Schoelkopf, R. J., and Devoret, M. H. (2006). Dispersive measurements of superconducting qubit coherence with a fast latching readout. *Physical Review B*, 73(5):054510.
- Siddiqi, I., Vijay, R., Pierre, F., Wilson, C. M., Metcalfe, M., Rigetti, C., Frunzio, L., and Devoret, M. H. (2004). RF-Driven Josephson bifurcation amplifier for quantum measurement. *Physical Review Letters*, 93(20):207002.
- Vijay, R., Slichter, D. H., and Siddiqi, I. (2011). Observation of quantum jumps in a superconducting artificial atom. *Physical Review Letters*, 106(11):110502.
- Vion, D., Aassime, A., Cottet, A., Joyez, P., Pothier, H., Urbina, C., Esteve, D., and Devoret, M. H. (2002). Manipulating the quantum state of an electrical circuit. *Science*, 296(5569):886–889.
- Wallraff, A., Schuster, D. I., Blais, A., Frunzio, L., Huang, R.-S., Majer, J., Kumar, S., Girvin, S. M., and Schoelkopf, R. J. (2004). Strong coupling of a single photon to a superconducting qubit using circuit quantum electrodynamics. *Nature*, 431(7005):162–167.